Electronic Supplementary Material (ESI) for Journal of Materials Chemistry A.

Electronic Supplementary Information

Hierarchically Porous Adamantane-Shaped Carbon Nanoframes

Sungeun Jeoung,[†,‡] *In Tae Ju,*[†,‡] *Jae Hyung Kim,*[§] *Sang Hoon Joo,**[*,§] *and Hoi Ri Moon**[*,†]

[†]Department of Chemistry and [§]School of Energy and Chemical Engineering, Ulsan National Institute of Science and Technology (UNIST), Ulsan 44919, Republic of Korea.

* e-mail: hoirimoon@unist.ac.kr, shjoo@unist.ac.kr

Experimental Details

Dye sorption experiments. The obtained carbon materials were investigated as adsorbents for large dye molecules such as rhodamine B (RhB), congo red (CR), and methylene blue (MB) in aqueous solution. Typically, a 10 mg adsorbent sample was sonically dispersed into 50 mL of an aqueous dye solution held in a 100 mL flask, and the mixture was stirred at 150 rpm on a heating plate. For dynamic adsorption measurements, 1.0 mL aliquots of the dispersion were sampled at a given time interval and filtered through a 0.2 μm syringe filter, with the concentration of the dye in the filtrate subsequently measured by UV-vis spectrophotometry.

Dynamic adsorption study. The amounts of dye adsorbed after n^{th} sampling (q_n) and at equilibrium (q_e) were calculated according to equations (1) and (2), respectively:

$$q_n = (c_0 - c_n) \text{ x } V_0 / m; \quad n = 1, 2, \ldots . \tag{1}$$

$$q_e = (c_0 - c_e) \text{ x } V_0 / m \tag{2}$$

where, c_0 (mg L^{-1}) is the initial dye concentration, c_n (mg L^{-1}) is the dye concentration after the n^{th} sampling, V_0 (L) is the initial solution volume, m (g) is the adsorbent mass, and c_e (mg L^{-1}) is the dye concentration in solution at adsorption equilibrium.

Adsorption kinetics study. Adsorption kinetics was fitted to pseudo-first-order and pseudo-second-order models, as shown in equations (3) and (4), respectively:

$$\ln(q_e - q_t) = \ln q_e - k_1 t \tag{3}$$

$$t / q_t = 1 / (k_2 q_e^2) + t / q_e \tag{4}$$

where q_t and q_e are the amounts of adsorbed dye (mg g^{-1}) at time t and at equilibrium, respectively, and k_1 (min^{-1}) and k_2 (g min^{-1} mg^{-1}) are the corresponding adsorption rate constants. The kinetic parameters obtained by linear regression analyses and the corresponding correlation coefficients (R^2) are listed in Table S2-4.

Adsorption isotherm study. Experimental adsorption data were fitted using Langmuir model, as shown in equations (5), respectively.

$$c_e / q_e = 1 / (K_L \text{ x } q_{max}) + c_e / q_{max} \tag{5}$$

where q_e and c_e are the amount of adsorbed dye (mg g^{-1}) and dye concentration (mg L^{-1}) in water at adsorption equilibrium, respectively, q_{max} (mg g^{-1}) is the maximum adsorption capacity, K_L (L mg^{-1}) is the Langmuir constant related to the binding energy between adsorbents and dye molecules. All obtained fitting parameters were shown in Table S2-S4.

Electrochemical measurements. Electrochemical analysis was performed by using a bipotentiostat (CHI760E, CH Instruments) and a rotator (AFMSRCE, Pine Research Instrumentation) in a three-electrode cell at room temperature. An Hg/HgO (CHI152, Ch Instruments; 1 M KOH filling solution) and a graphite rod were used as the reference and the counter electrode, respectively. 0.1 M KOH electrolyte was prepared by dissolving 99.99% KOH pellet (Aldrich) in deionized (DI) water (Millipore Milli-Q system, 18.2 MΩ·cm). To report potential with respect to a reversible hydrogen electrode (RHE), a reduction potential difference between the Hg/HgO electrode and the RHE was obtained by constructing a two-electrode cell. A Pt coil and the Hg/HgO electrode were immersed in an electrolyte, and H_2 gas was purged for 20 minutes. Since the Pt coil can be considered as the RHE, RHE conversion value could be taken by an open circuit potential. A RRDE (AFE7R9GCPT, Pine Research Instrumentation) coated with a catalyst ink was used as the working electrode. Prior to the measurement, the RRDE was polished with 1.0 μm and 0.3 μm alumina suspensions sequentially to obtain a mirror finish. For the preparation of the catalyst ink, 15 mg of catalyst powder, 50 μL of DI water, 37.5 μL of Nafion (5 wt% in isopropanol and water, D521, DuPont), and 505 μL of dry ethanol (Samchun) were ultrasonicated for 30 minutes. For Pt/C catalyst (20 wt% Pt, HiSPEC-3000, Johnson-Matthey), a catalyst ink was prepared by mixing 3.5 mg of Pt/C, 100 μL of DI water, 30 μL of Nafion, and 1070 μL of dry ethanol. From the prepared catalyst ink, 6 μL was pipetted onto the glassy carbon (0.247 cm^{-2}) of the RRDE, resulting in a 0.6 mg cm^{-2} catalyst loading (14 μg_{Pt} cm^{-2} for Pt/C). Before evaluating electrocatalytic properties, electrochemical cleaning was performed in advance by cyclic voltammetry (CV) in a potential range from 0.05 V to 1.2 V for 20 cycles at a scan rate of 100 mV s^{-1} in the N_2-saturated condition (50 cycles, 500 mV s^{-1} for Pt/C). Subsequently, CV was carried out in the same potential range for 3 cycles at a scan rate of 20 mV s^{-1} (50 mV s^{-1} for Pt/C) . ORR polarization curves were obtained by linear sweep voltammetry (LSV) from 1.2 V to 0.2 V (-0.01 V – 1.1 V for Pt/C) at a scan rate of 5 mV s^{-1} (20 mV s^{-1} for Pt/C) at a rotating speed of 1600 rpm in the O_2-saturated condition. Non-faradaic current was corrected by conducting same LSV procedure in N_2-saturated condition, and subtracting LSV data collected in N_2-saturated condition from that in O_2-saturated condition. To obtain a solution resistance for *iR*-compensation, electrochemical impedance spectra was achieved at 0.68 V with AC potential amplitude of 10 mV from 100,000 to 1 Hz. An intercept of X-axis from a Nyquist plot was determined as the solution resistance. ORR polarization curves were displayed after *iR*-compensation. Kinetic current was calculated by equation (6):

$$1 / i_d = 1 / i_k + 1 / i_l \tag{6}$$

where i_d, i_k, and i_l are the disk current, the kinetic current, and diffusion-limited current, respectively. Electron transfer number (n) and HO_2^- yield were calculated by the following equations (7) and (8), respectively:

$$n = 200/(1 + (N \times i_d)/i_r) \tag{7}$$

$$HO_2^- \text{ yield } (\%) = 4/(1 + i_r/(N \times i_r) \tag{8}$$

where N and i_r represents the collection efficiency (0.37, provided by manufacturer) and the ring current. The ring current was obtained by applying 1.3 V to Pt ring during LSV in O_2-saturated condition. Tafel plots were acquired by the following equation (9):

$$E = -b\log(i_k) + C \tag{9}$$

where E, b, and C stand for the applied potential, the Tafel slope, and the constant. All the displayed data were average values after 3 times measurement.

Table S1. The adsorption dynamic parameters and Langmuir constants of *m*-NC and *mM*-NC-200 for RhB molecules.

Adsorbent	Pseudo-second-order			Langmuir model		
	k_2 *10^3 (g mg^{-1} min^{-1})	$q_{e,cal}$ (mg g^{-1})	R^2	q_{max} (mg g^{-1})	K_L (L mg^{-1})	R^2
m-NC	7.49	39	0.9978	45.0	0.159	0.9977
mM-NC-200	20.0	216	0.9997	397	0.229	0.9851

Table S2. The adsorption dynamic parameters and Langmuir constants of *m*-NC and *mM*-NC-200 for CR molecules.

Adsorbent	Pseudo-second-order			Langmuir model		
	k_2 *10^3 (g mg^{-1} min^{-1})	$q_{e,cal}$ (mg g^{-1})	R^2	q_{max} (mg g^{-1})	K_L (L mg^{-1})	R^2
m-NC	6.36	14	0.9992	35.7	0.021	0.9417
mM-NC-200	17.7	232	0.9999	400	0.167	0.9909

Table S3. The adsorption dynamic parameters and Langmuir constants of *m*-NC and *mM*-NC-200 for MB molecules.

Adsorbent	Pseudo-second-order			Langmuir model		
	$k_2 *10^3$ (g mg^{-1} min^{-1})	$q_{e,cal}$ (mg g^{-1})	R^2	q_{max} (mg g^{-1})	K_L (L mg^{-1})	R^2
m-NC	2.04	86	0.9847	140	0.074	0.9872
mM-NC-200	6.61	256	0.9999	500	0.667	0.9989

Table S4. Summary of half-wave potentials, kinetic current densities, and diffusion-limited current densities of *m*-NC and *mM*-NC-200 for ORR.

Catalyst	Half-wave potential (V)[a)]	Kinetic current density @ 0.8 V (mA cm^{-2})	Diffusion-limited current density @ 0.3 V (mA cm^{-2})
m-NC	0.705	0.53	4.7
mM-NC-200	0.784	7.6	6.0

[a)] Potentials at −3 mA cm^{-2} of LSV polarization curves

Table S5. Comparison table of adsorption performance for large dye molecules by porous carbon based adsorbents.

Reference	Adsorbent	Dye	Initial adsorption rate / dye concentration	$q_{\max}$ (mg g^{-1})
This work	*mM*-NC-200	Rhodamine B	199 mg g^{-1} (10 min) / 50 mg L^{-1}	397
		Congo red	218 mg g^{-1} (10 min) / 50 mg L^{-1}	400
		Methylene blue	238 mg g^{-1} (10 min) / 50 mg L^{-1}	500
1	Gelatin/activated carbon composite beads	Rhodamine B	~64 mg g^{-1} (9 min) / 100 mg L^{-1}	244
2	Fibrous N-doped hierarchical porous carbon microsphere	Rhodamine B	~26 mg g^{-1} (10 min) / 47.8 mg L^{-1}	140
3	Tannic acid functionalized graphene	Rhodamine B	~45 mg g^{-1} (30 min) / 64.0 mg L^{-1}	201
4	Hierarchically porous tubular carbon (HPTC) Activated HPTC	Methylene blue	-	331
5	Activated carbon	Methylene blue	~96 mg g^{-1} (60 min) / 100 mg L^{-1}	294
6	Carbon nanotube	Methylene blue	~14 mg g^{-1} (60 min) / 20 mg L^{-1}	46.2
7	Activated carbon from oil palm wood	Methylene blue	-	90.9

Table S6. Comparison of ORR activity parameters of *mM*-NC-200 with previously reported MOF-derived N-doped carbons.

Reference	Catalyst	Half-wave potential (V)	Diffusion-limited current density (mA cm^{-2})[a]
This work	*mM*-NC-200	0.784	6.0
8	NC900	0.66	3.9
9	NGPC-1000-10	0.77	4.69
10	GNPCSs-800	0.81	6.0
11	Carbon L	0.697	4.59
12	$Zn(elm)_2$ PTIP	0.78	5.1
13	MOFCN-900	0.76	4.2
14	NEMC/G	0.822	4.84
15	NCNTFs	0.87	5.3
16	PNPN-1000	0.76	6.9
17	EZIF-C	0.78	6.3

[a] at a rotation speed of 1600 rpm

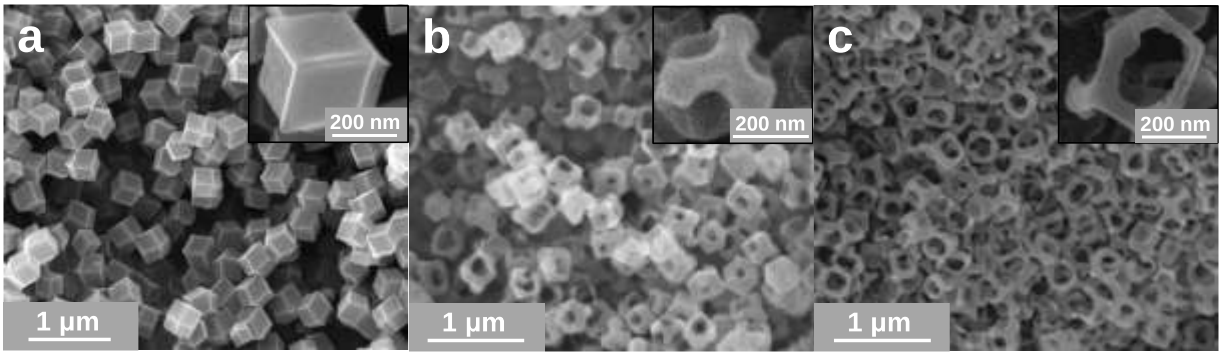

Figure S1. SEM images of ZIF-8 and chemically etched ZIF-8. (a) ZIF-8, (b) *M*-ZIF-8-100, and (c) *M*-ZIF-8-200.

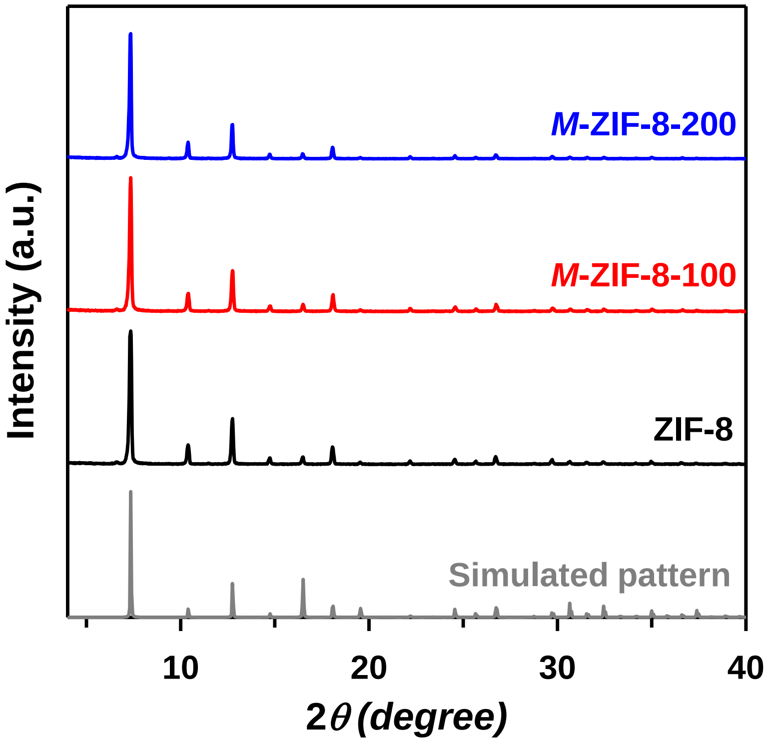

Figure S2. XRPD patterns of ZIF-8, *M*-ZIF-8-100, and *M*-ZIF-8-200.

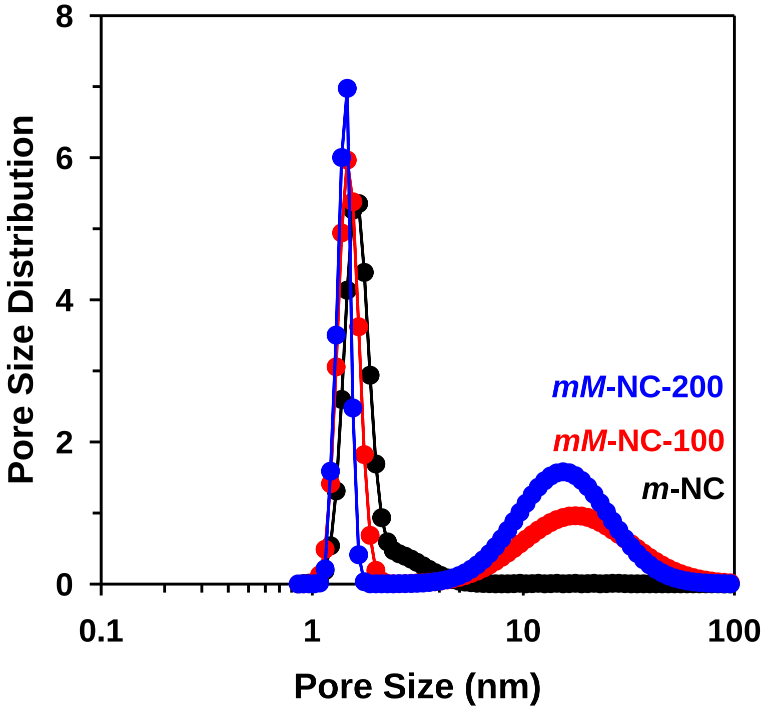

Figure S3. NLDFT pore size distribution curves of *m*-NC, *mM*-NC-100, and *mM*-NC-200.

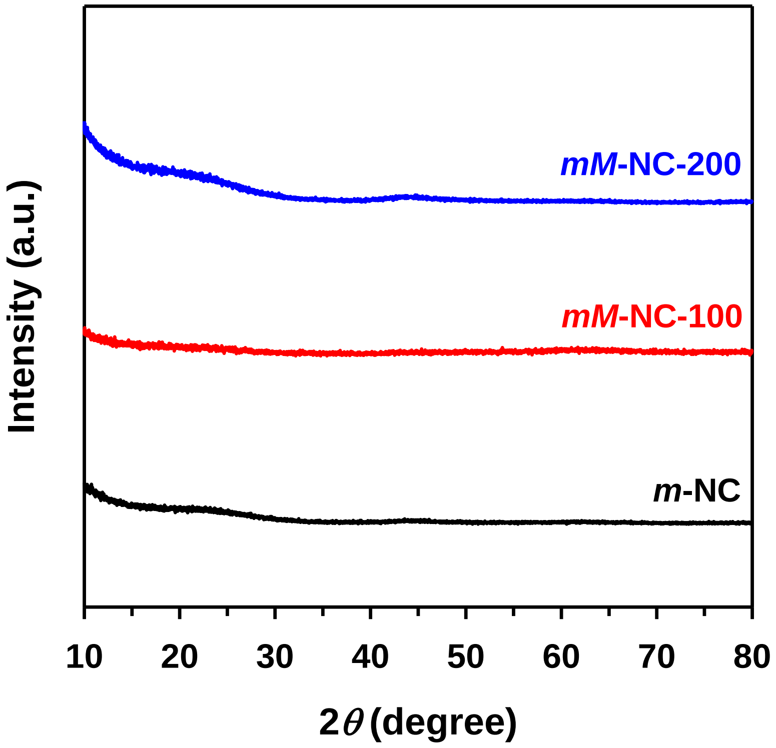

Figure S4. XRPD patterns of *m*-NC, *mM*-NC-100, and *mM*-NC-200.

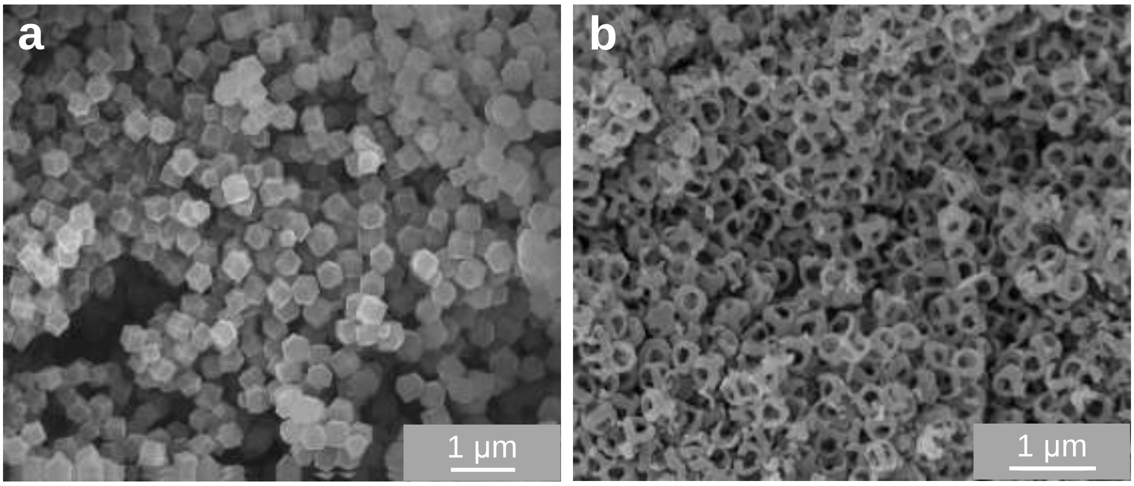

Figure S5. SEM images of (a) ZIF-67 and (b) *M*-ZIF-67.

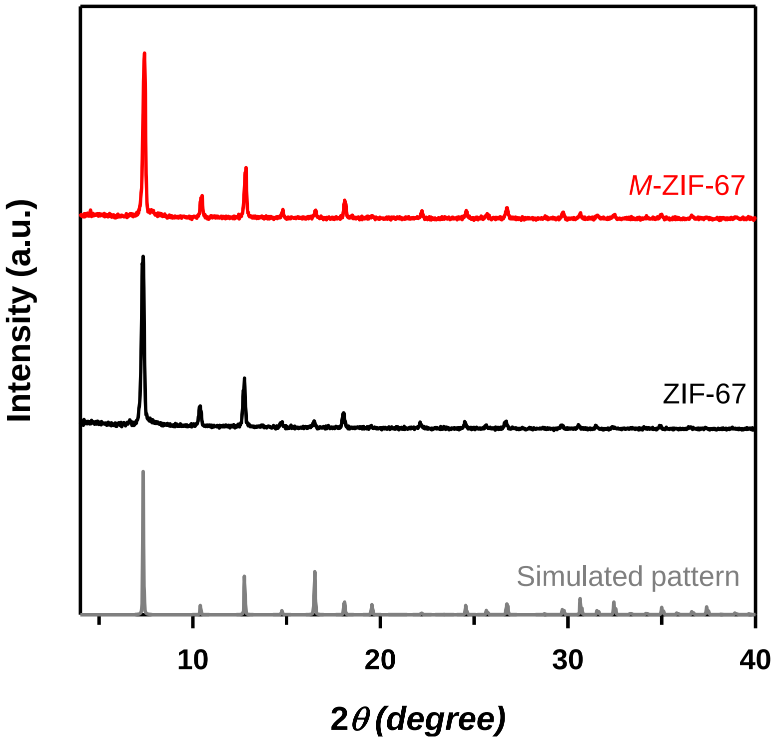

Figure S6. XRPD patterns of ZIF-67 and *M*-ZIF-67.

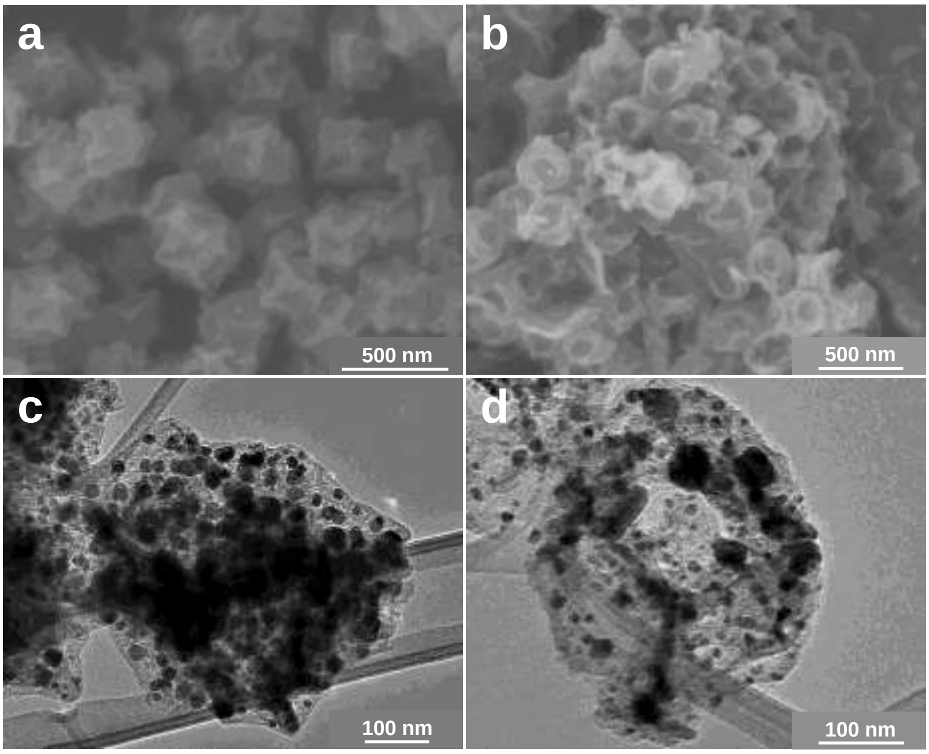

Figure S7. Morphologies and structures of ZIF-67-derived cobalt-doped carbon materials. SEM images of (a) *m*-CoNC and (b) *mM*-CoNC. TEM images of (c) *m*-CoNC and (d) *mM*-CoNC. While direct thermolysis of ZIF-67 yields Co NP embedded, microporous, N-doped carbon, *m*-CoNC, *M*-ZIF-67 is converted to Co nanoparticle (NP) embedded, hierarchically porous, N-doped carbon, *mM*-CoNC.

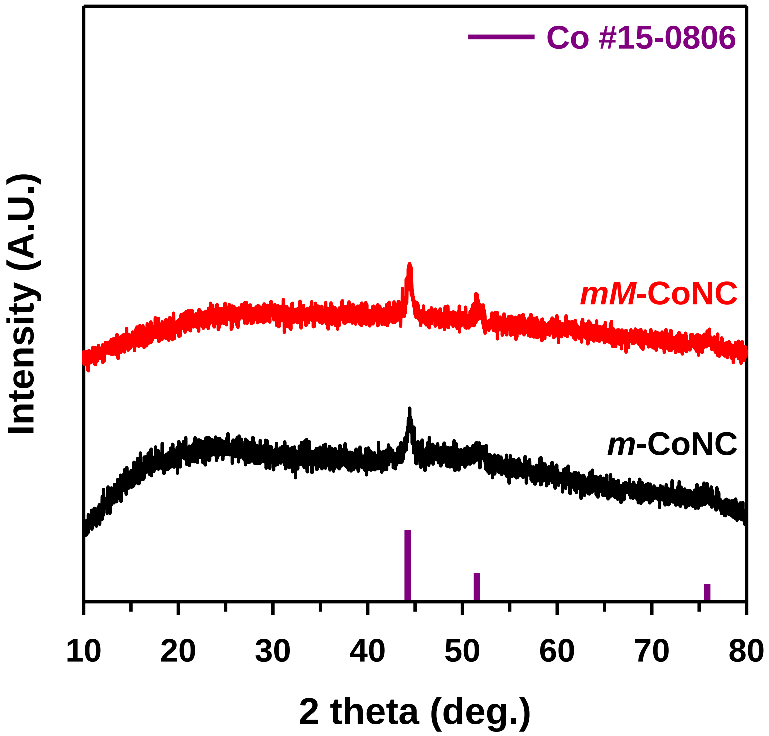

Figure S8. XRPD patterns of *m*-CoNC and *mM*-CoNC.

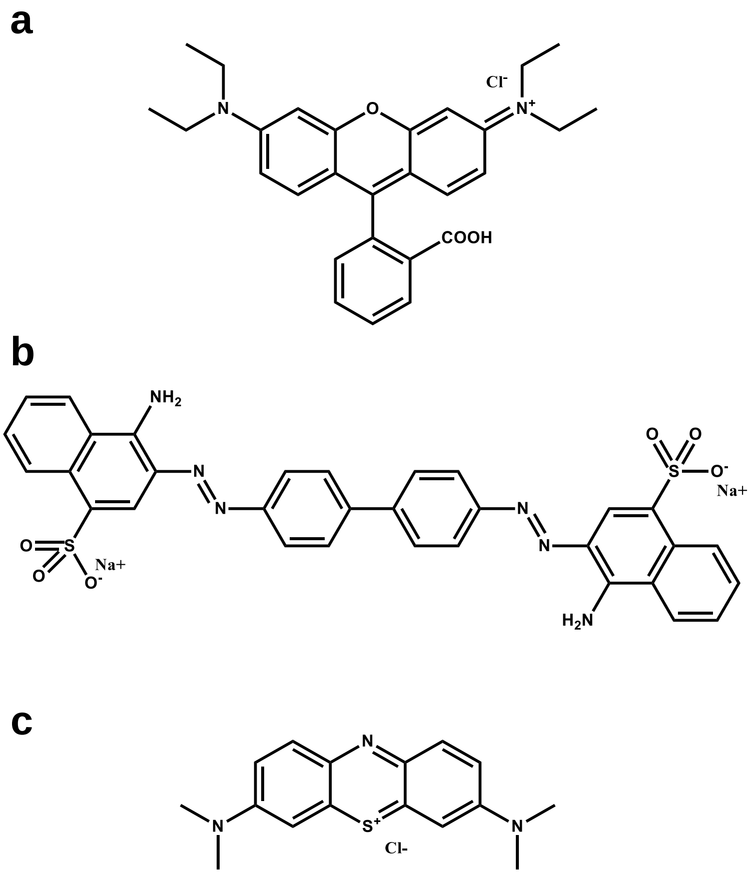

Figure S9. Dye molecules: (a) rhodamine B (RhB), (b) congo red (CR), and (c) methylene blue (MB).

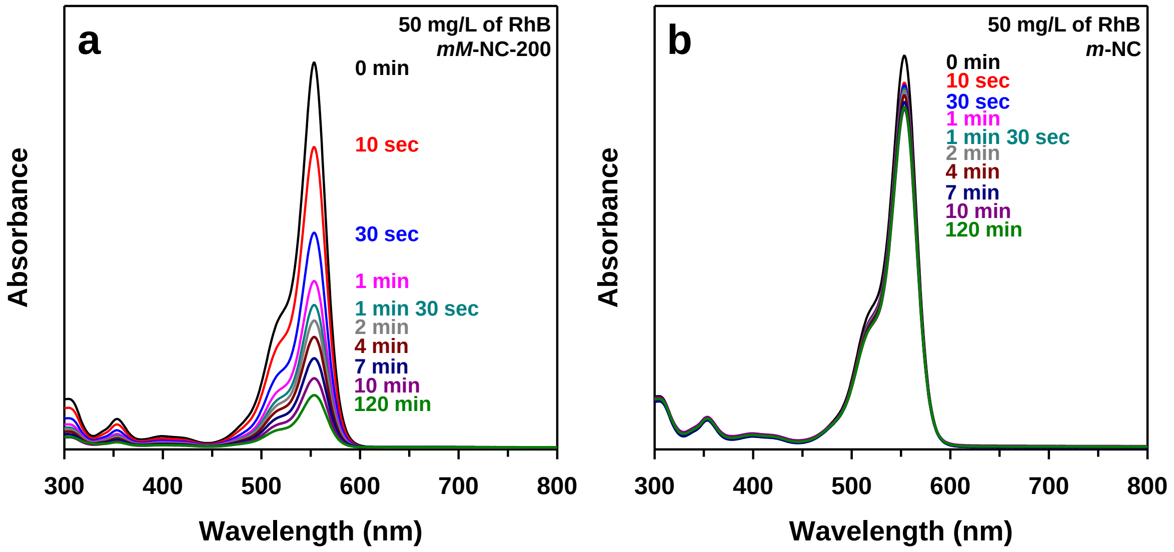

Figure S10. UV-vis absorption spectra of an aqueous solution of RhB (50.0 mg/L) after dye adsorption with (a) *mM*-NC-200 and (b) *m*-NC at different interval time.

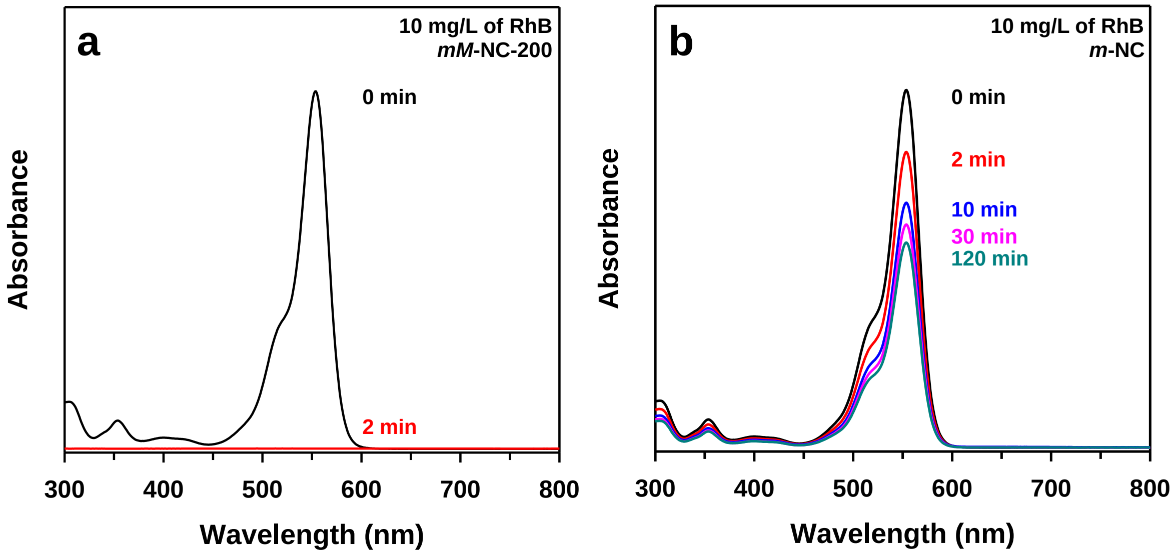

Figure S11. UV-vis absorption spectra of an aqueous solution of RhB (10.0 mg/L) after dye adsorption with (a) *mM*-NC-200 and (b) *m*-NC at different interval time.

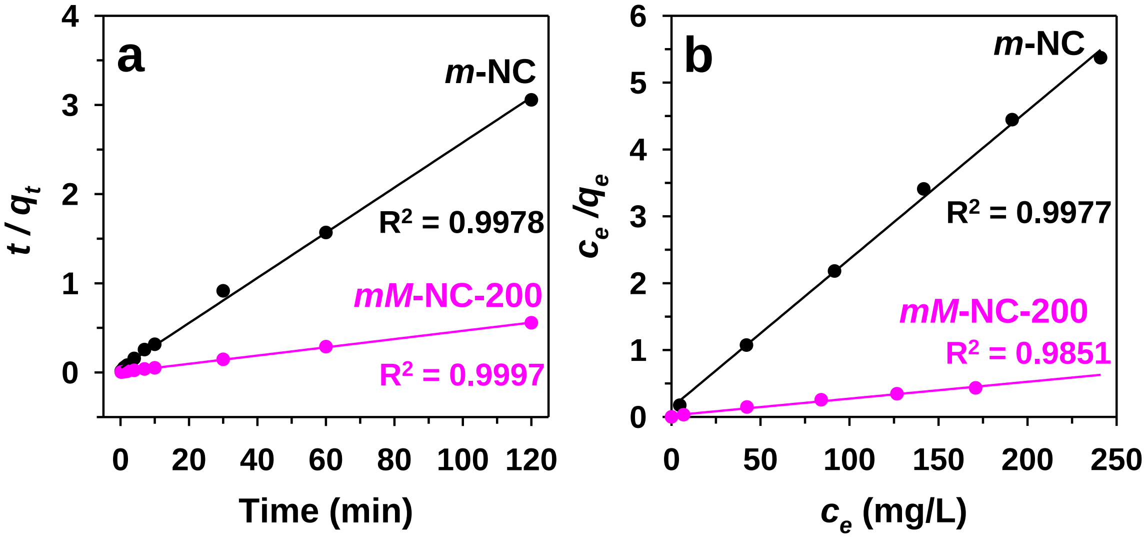

Figure S12. (a) t/q_t versus t plots derived from Figure 3a and fitted using the pseudo-second-order model. (b) c_e/q_e versus c_e plots derived from Figure 3b and fitted using the Langmuir model.

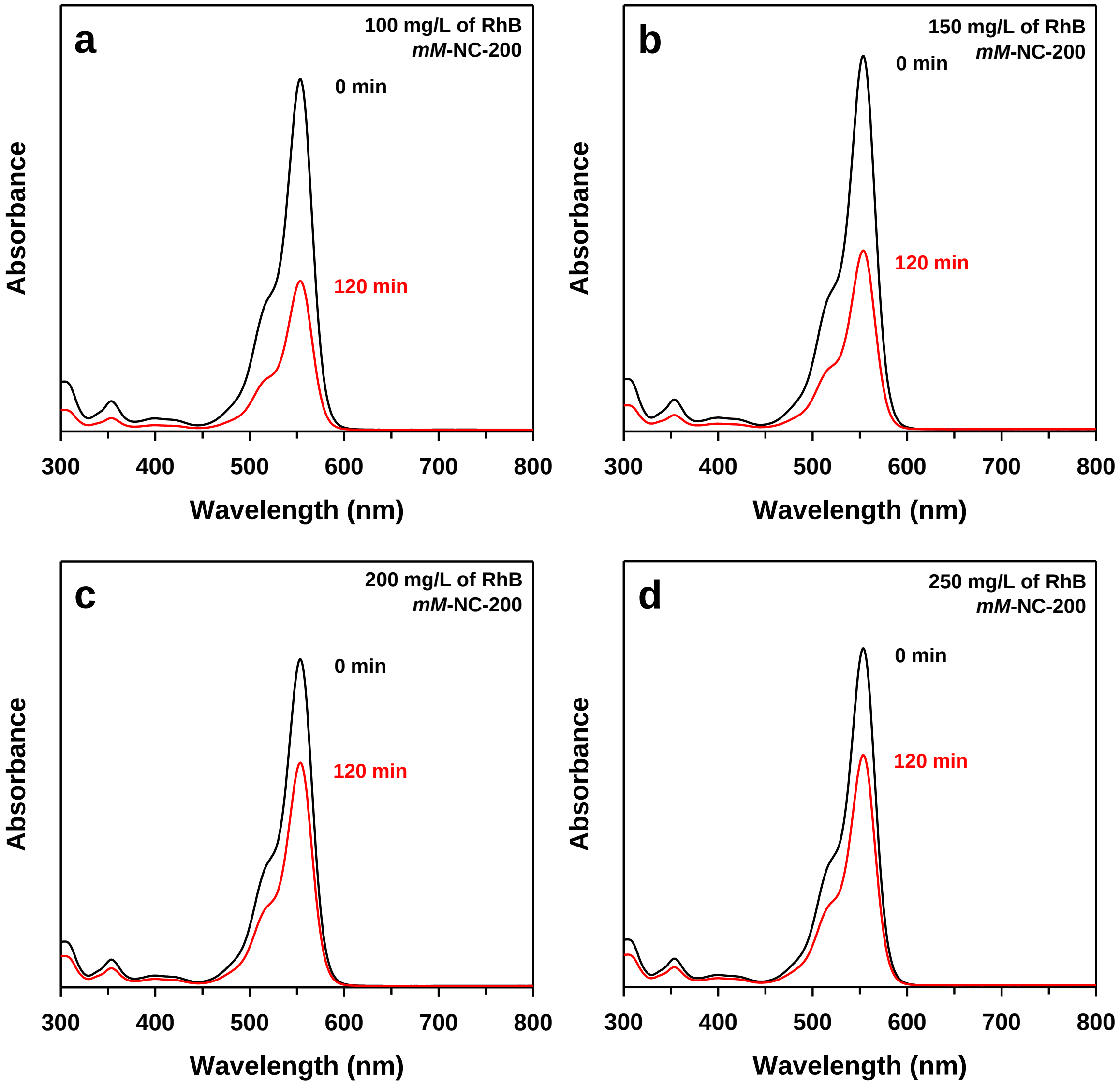

Figure S13. UV-vis absorption spectra of various concentrations of RhB aqueous solutions, (a) 100 mg/L, (b) 150 mg/L, (c) 200 mg/L, and (d) 250 mg/L after dye adsorption with *mM*-NC-200.

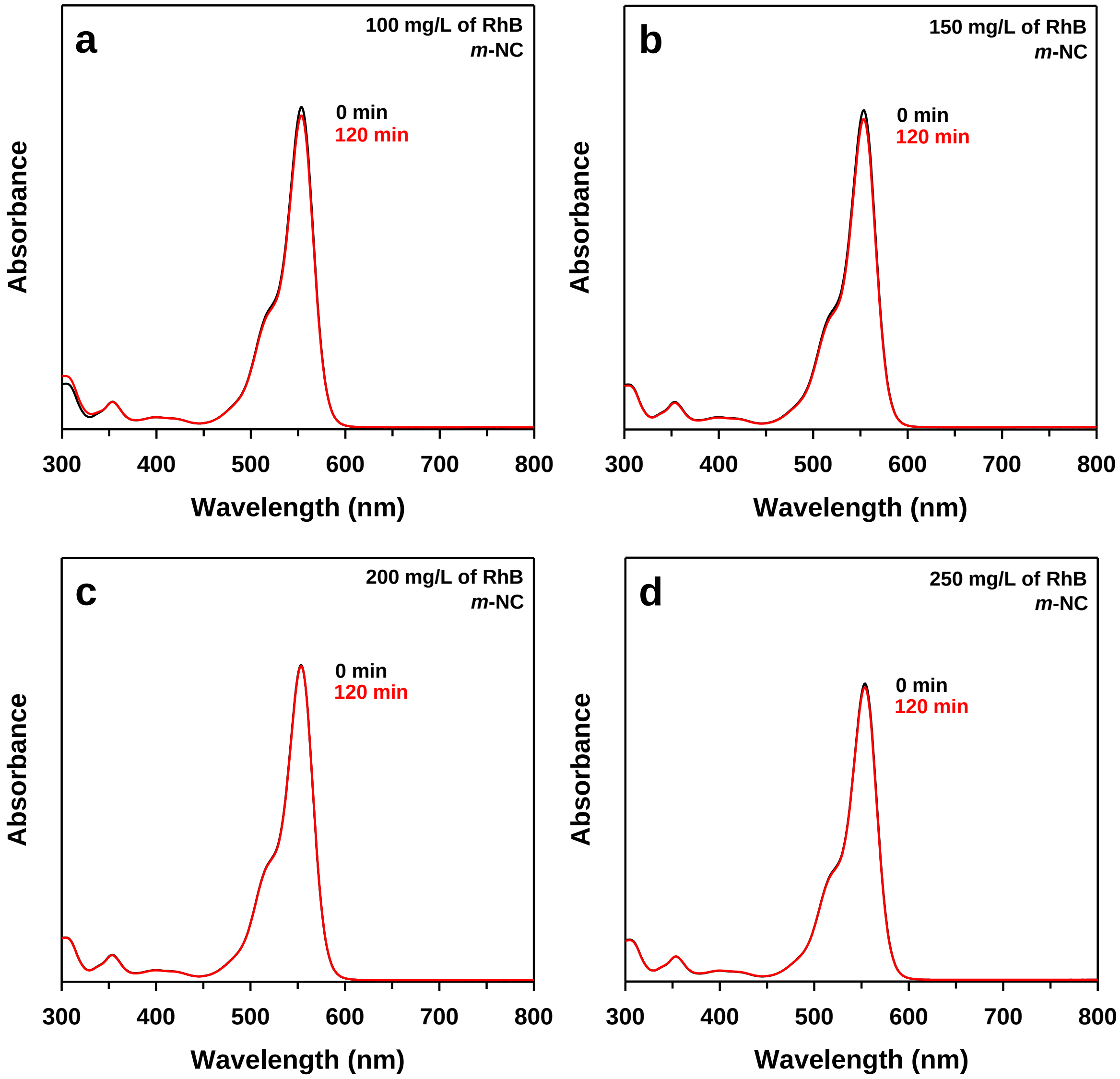

Figure S14. UV-vis absorption spectra of various concentrations of RhB aqueous solutions, (a) 100 mg/L, (b) 150 mg/L, (c) 200 mg/L, and (d) 250 mg/L after dye adsorption with *m*-NC.

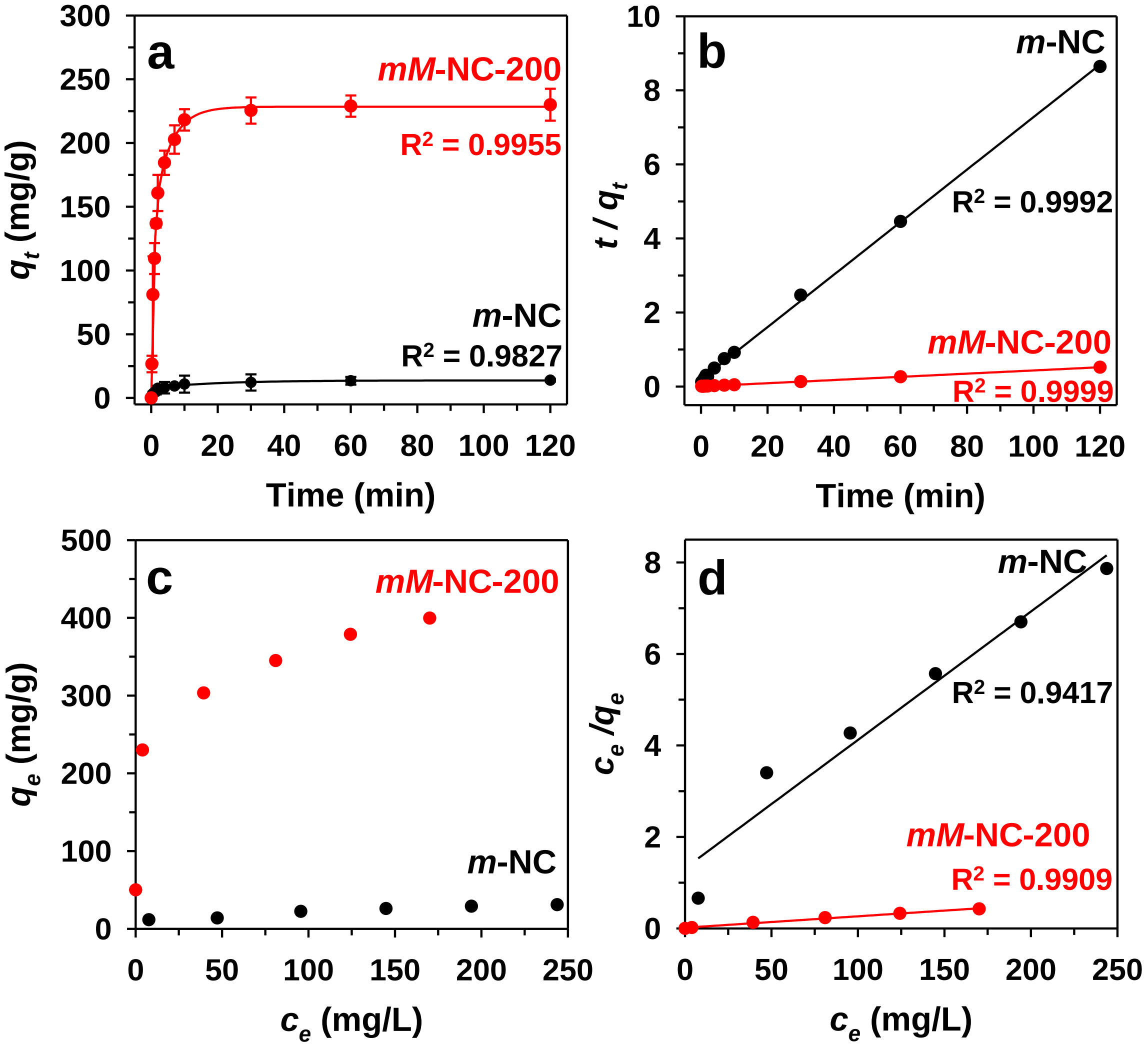

Figure S15. (a) Dynamic curves for CR (50.0 mg L^{-1}) adsorption onto *mM*-NC-200 and *m*-NC. (b) t/q_t versus t plots derived from (a) and fitted using the pseudo-second-order model. (c) Isotherms for CR (10-250 mg L^{-1}) adsorption onto *mM*-NC-200 and *m*-NC. (d) c_e/q_e versus c_e plots derived from (c) and fitted using the Langmuir model.

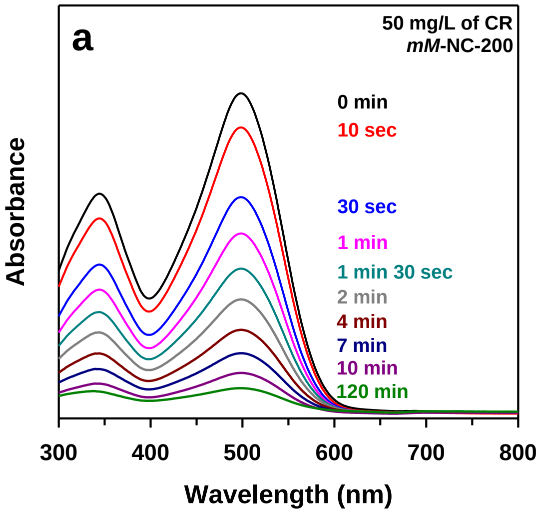

Figure S16. UV-vis absorption spectra of an aqueous solution of CR (50.0 mg/L) after dye adsorption with (a) *mM*-NC-200 and (b) *m*-NC at different interval time.

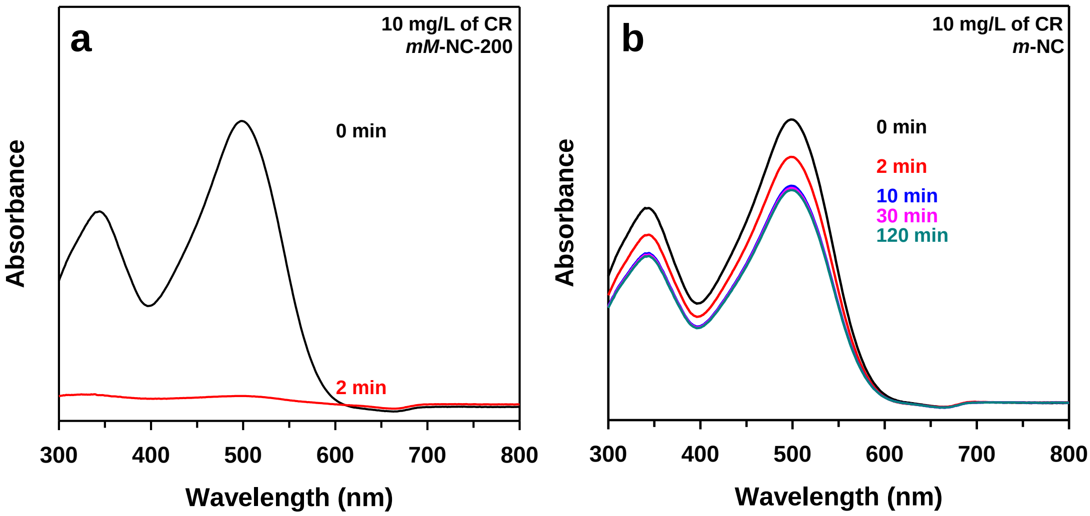

Figure S17. UV-vis absorption spectra of an aqueous solution of CR (10.0 mg/L) after dye adsorption with (a) *mM*-NC-200 and (b) *m*-NC at different interval time.

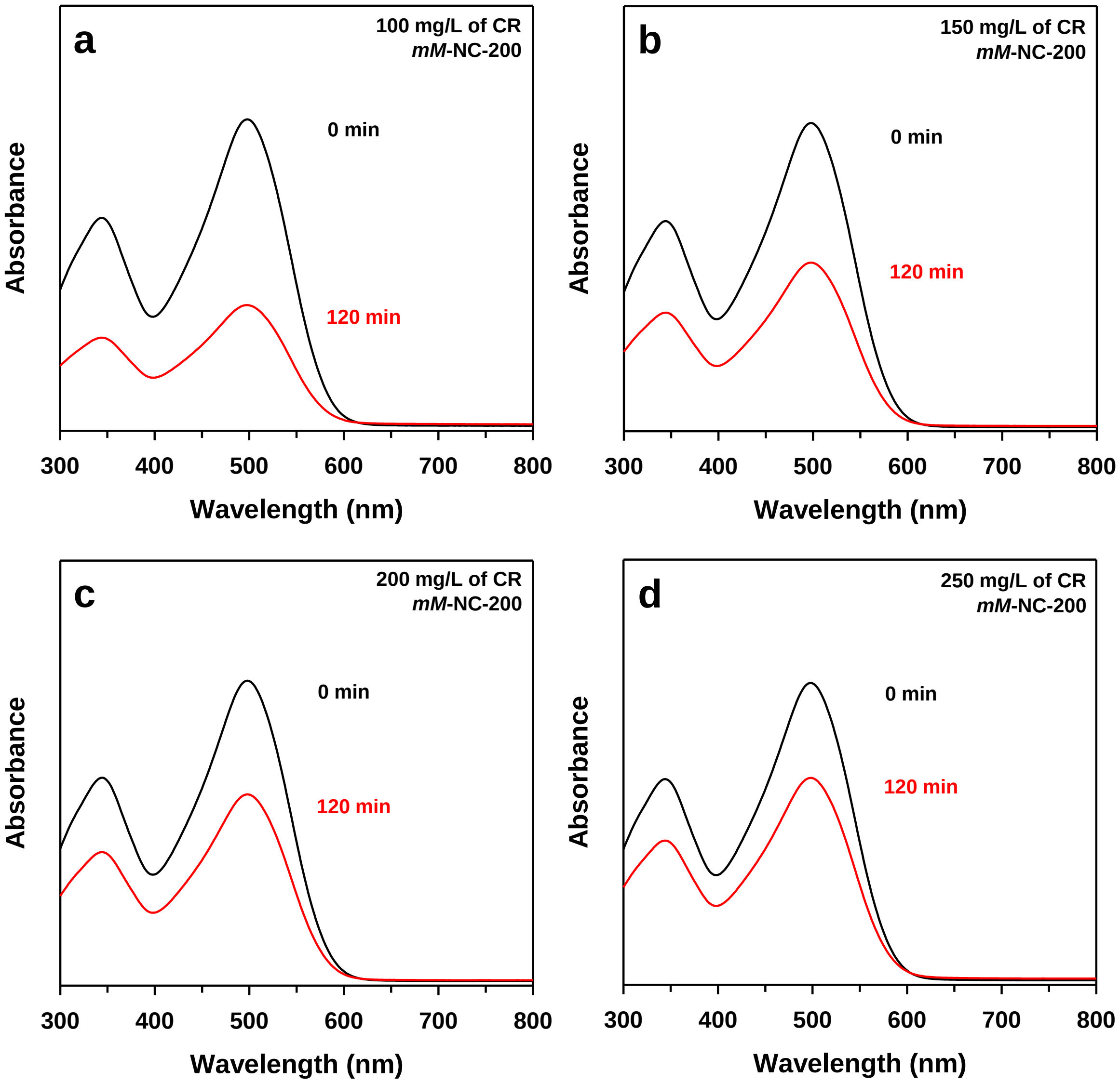

Figure S18. UV-vis absorption spectra of various concentrations of CR aqueous solutions, (a) 100 mg/L, (b) 150 mg/L, (c) 200 mg/L, and (d) 250 mg/L after dye adsorption with *mM*-NC-200.

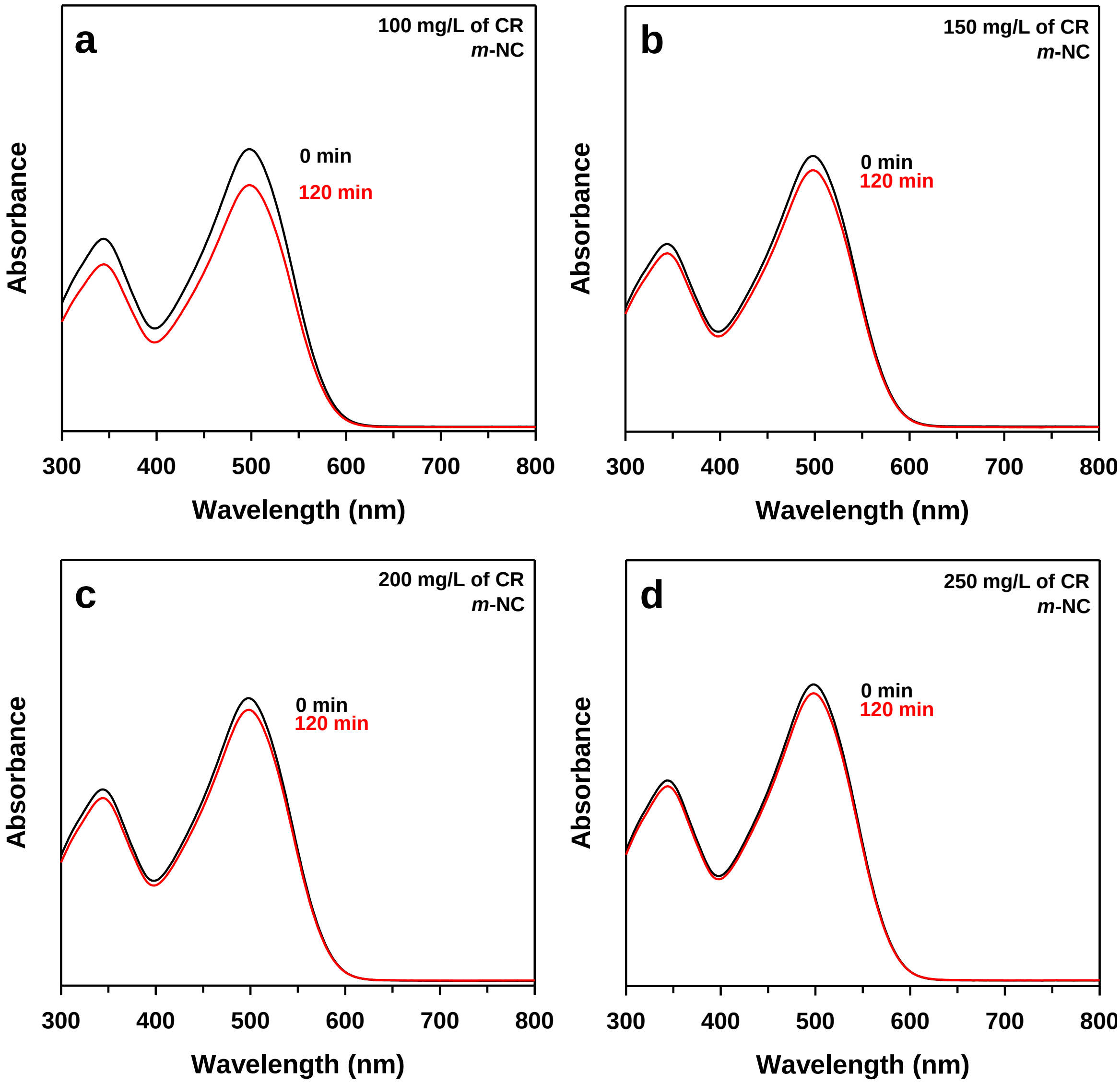

Figure S19. UV-vis absorption spectra of various concentrations of CR aqueous solutions, (a) 100 mg/L, (b) 150 mg/L, (c) 200 mg/L, and (d) 250 mg/L after dye adsorption with *m*-NC.

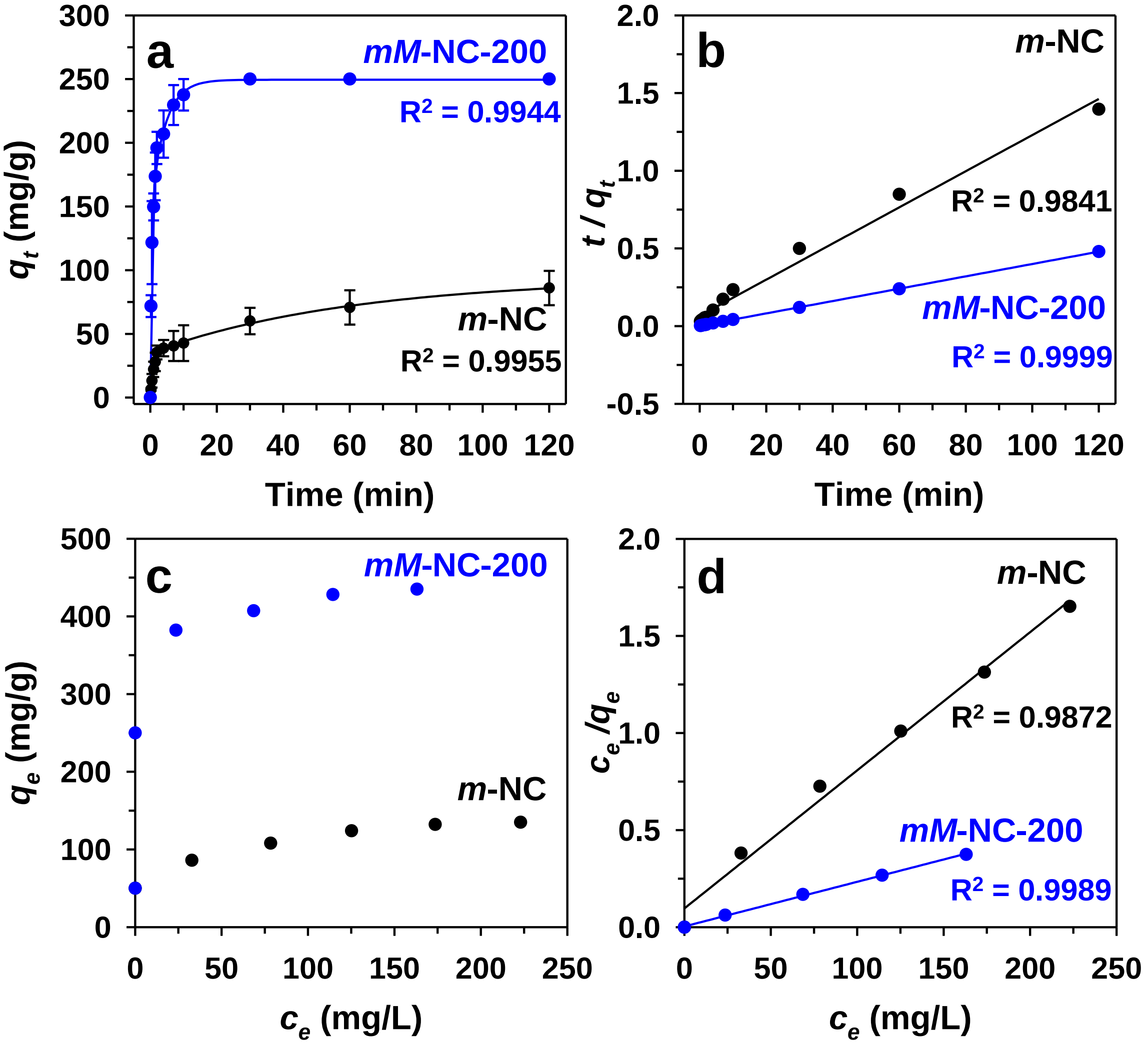

Figure S20. (a) Dynamic curves for MB (50.0 mg L^{-1}) adsorption onto *mM*-NC-200 and *m*-NC. (b) t/q_t versus t plots derived from (a) and fitted using the pseudo-second-order model. (c) Isotherms for MB (10-250 mg L^{-1}) adsorption onto *mM*-NC-200 and *m*-NC. (d) c_e/q_e versus c_e plots derived from (c) and fitted using the Langmuir model.

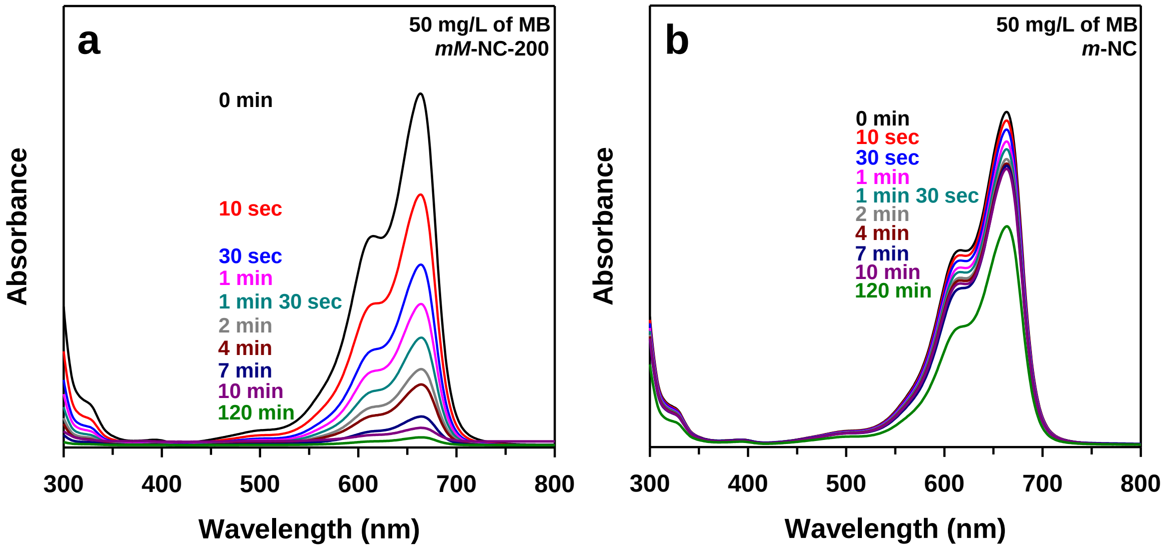

Figure S21. UV-vis absorption spectra of an aqueous solution of MB (50.0 mg/L) after dye adsorption with (a) *mM*-NC-200 and (b) *m*-NC at different interval time.

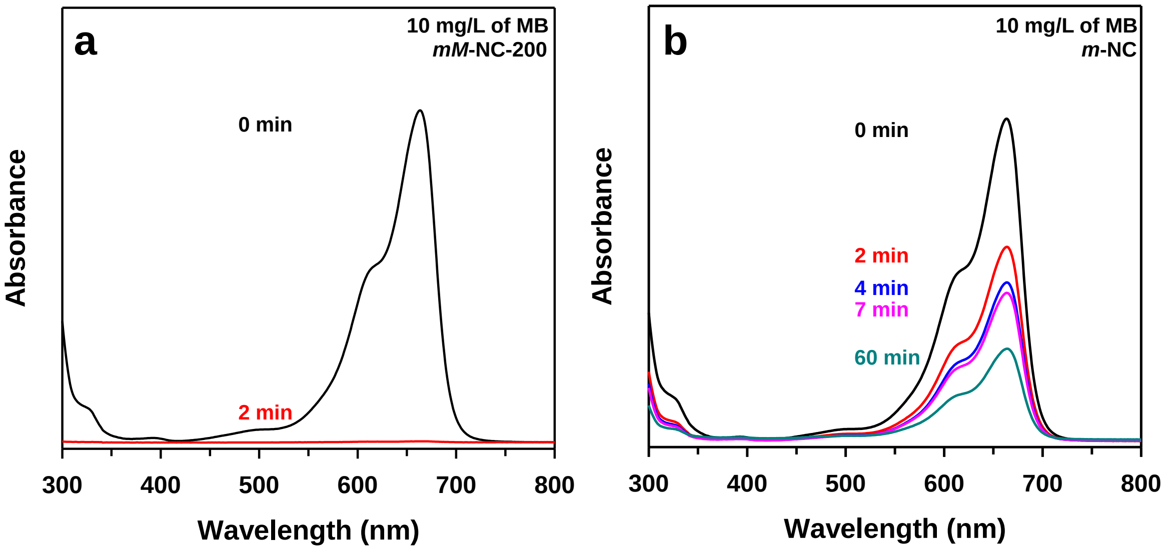

Figure S22. UV-vis absorption spectra of an aqueous solution of MB (10.0 mg/L) after dye adsorption with (a) *mM*-NC-200 and (b) *m*-NC at different interval time.

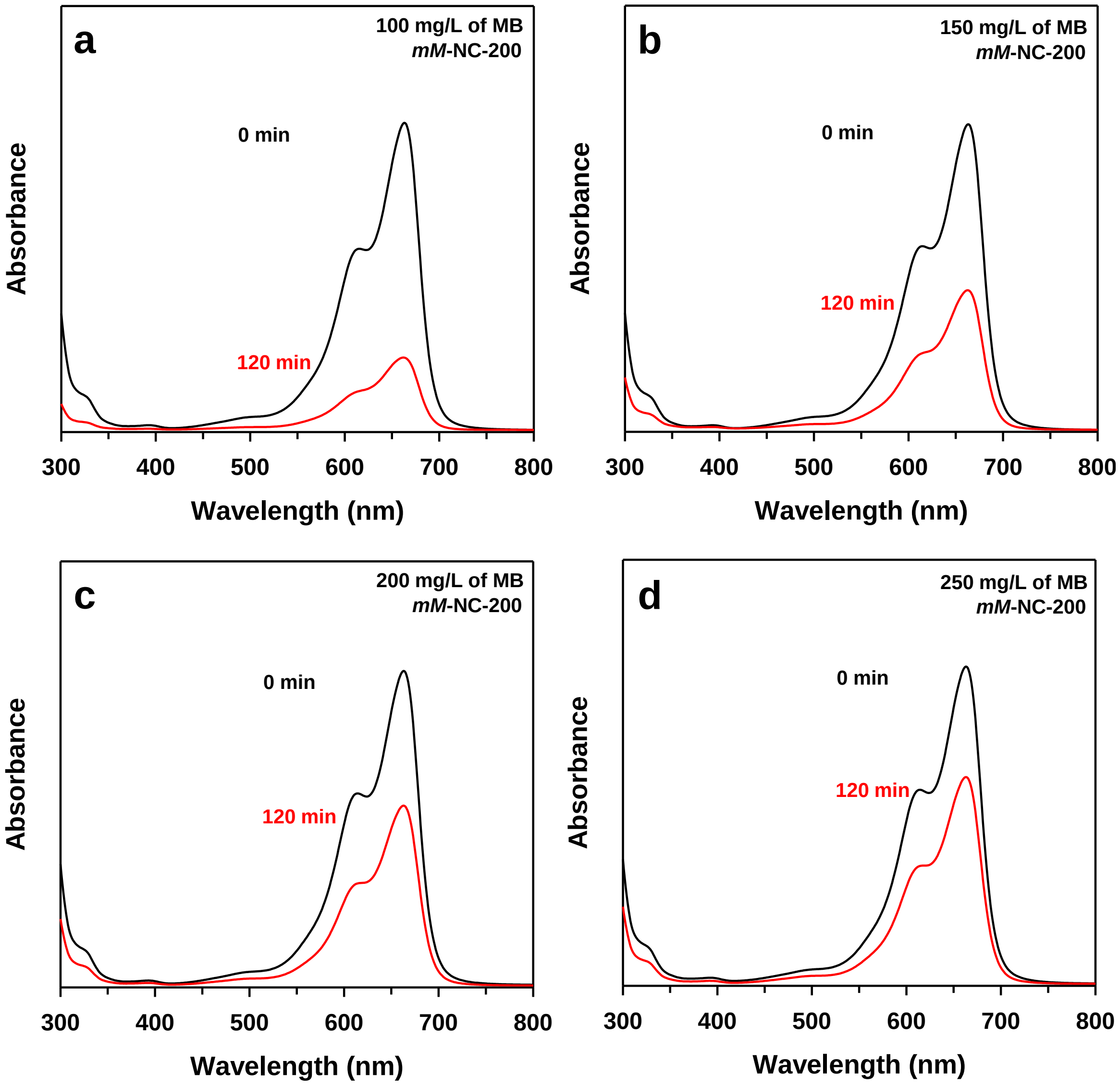

Figure S23. UV-vis absorption spectra of various concentrations of MB aqueous solutions, (a) 100 mg/L, (b) 150 mg/L, (c) 200 mg/L, and (d) 250 mg/L after dye adsorption with *mM*-NC-200.

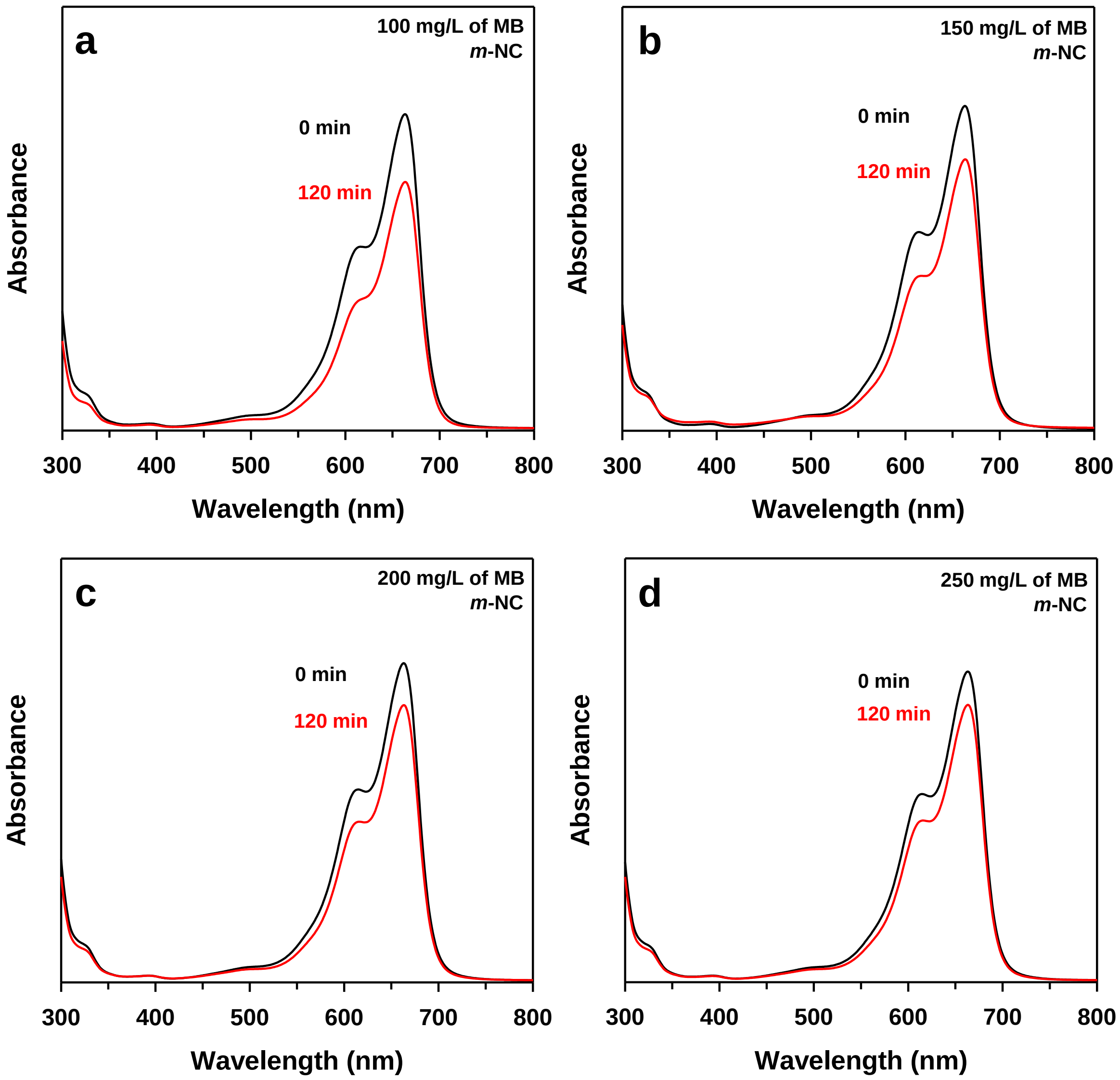

Figure S24. UV-vis absorption spectra of various concentrations of MB aqueous solutions, (a) 100 mg/L, (b) 150 mg/L, (c) 200 mg/L, and (d) 250 mg/L after dye adsorption with *m*-NC.

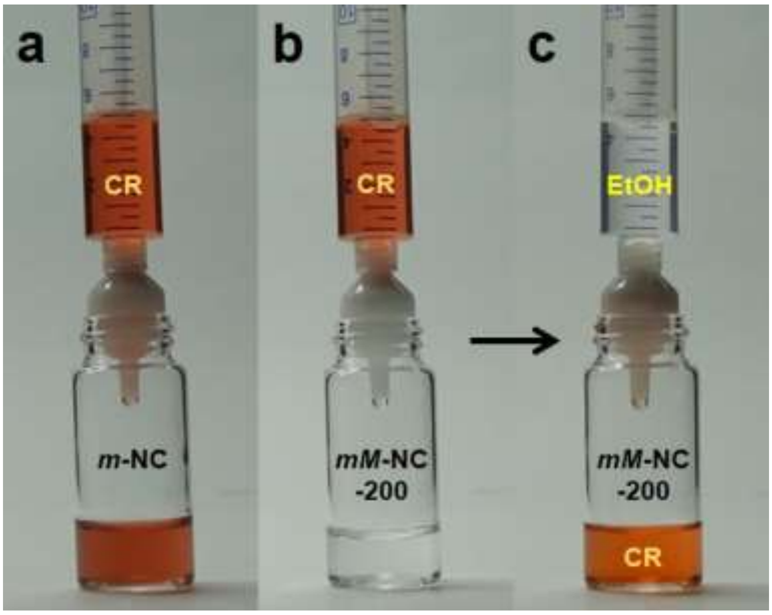

Figure S25. Application of carbon thin films in dye filtration. Filtration performance of (a) *m*-NC and (b) *mM*-NC-200 thin films tested using aqueous CR (10 mg L^{-1}). (c) Regeneration of *mM*-NC-200 using ethanol.

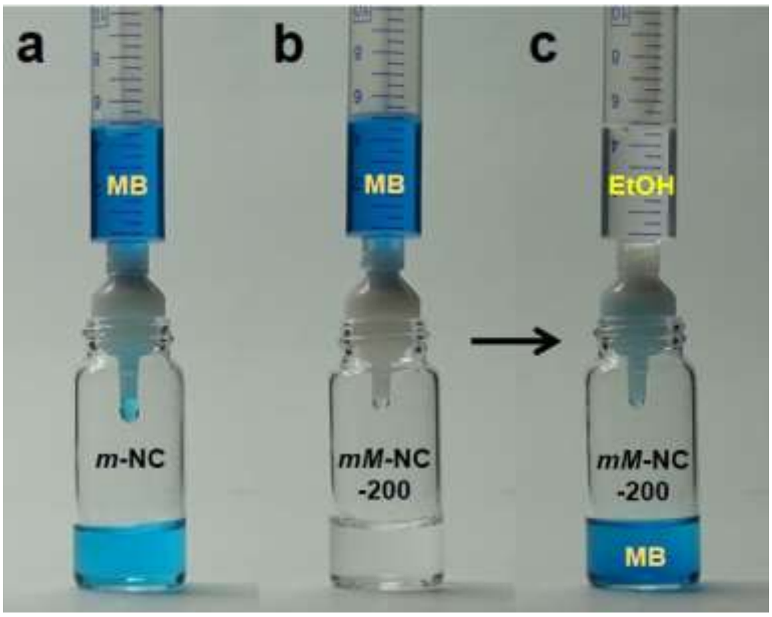

Figure S26. Application of carbon thin films in dye filtration. Filtration performance of (a) *m*-NC and (b) *mM*-NC-200 thin films tested using aqueous MB (10 mg L^{-1}). (c) Regeneration of *mM*-NC-200 using ethanol.

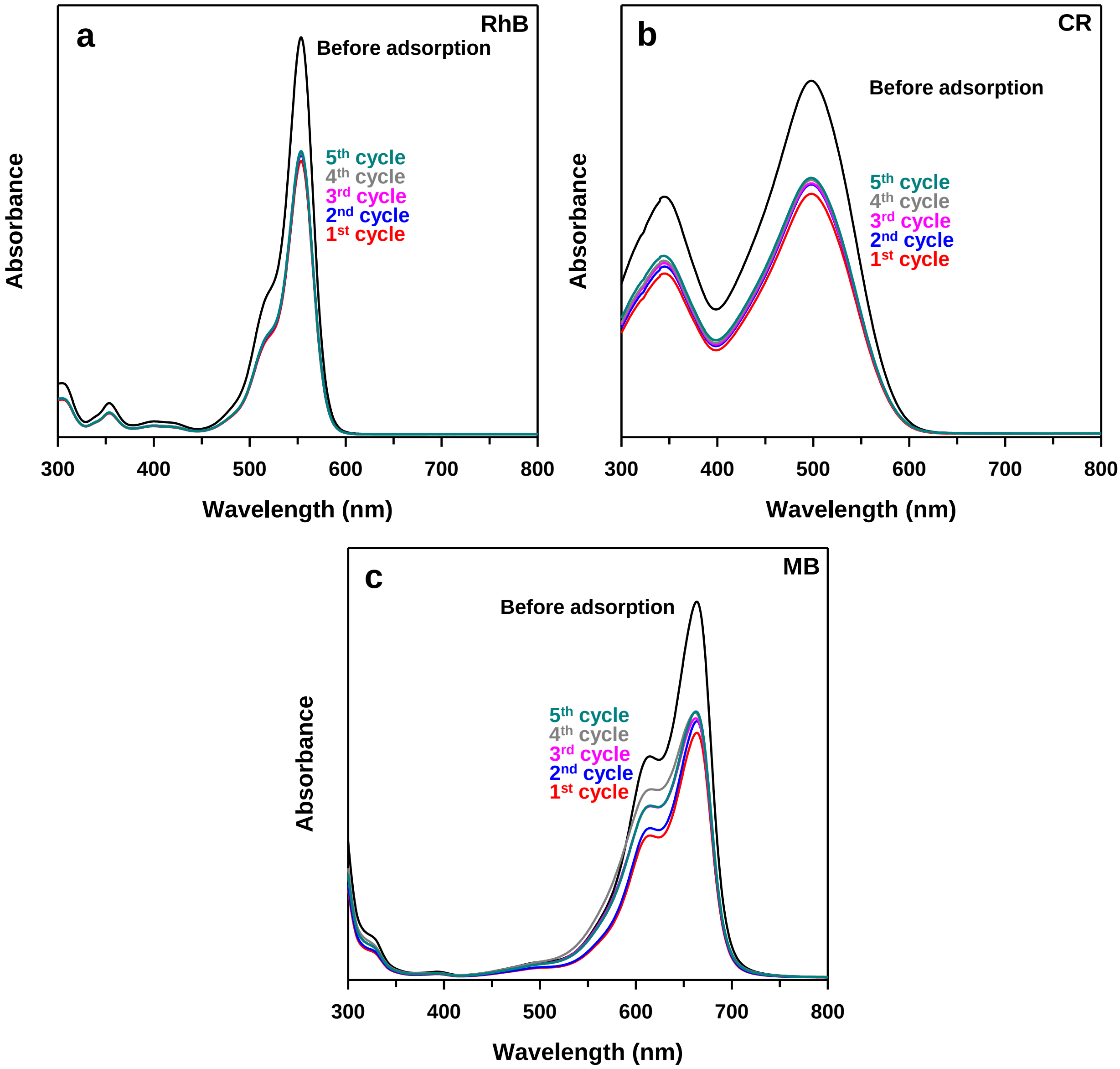

Figure S27. UV-vis absorption spectra of 250 mg L^{-1} aqueous dye solutions of (a) RhB, (b) CR, and (c) MB during five cycles of dye adsorption/regeneration with *mM*-NC-200.

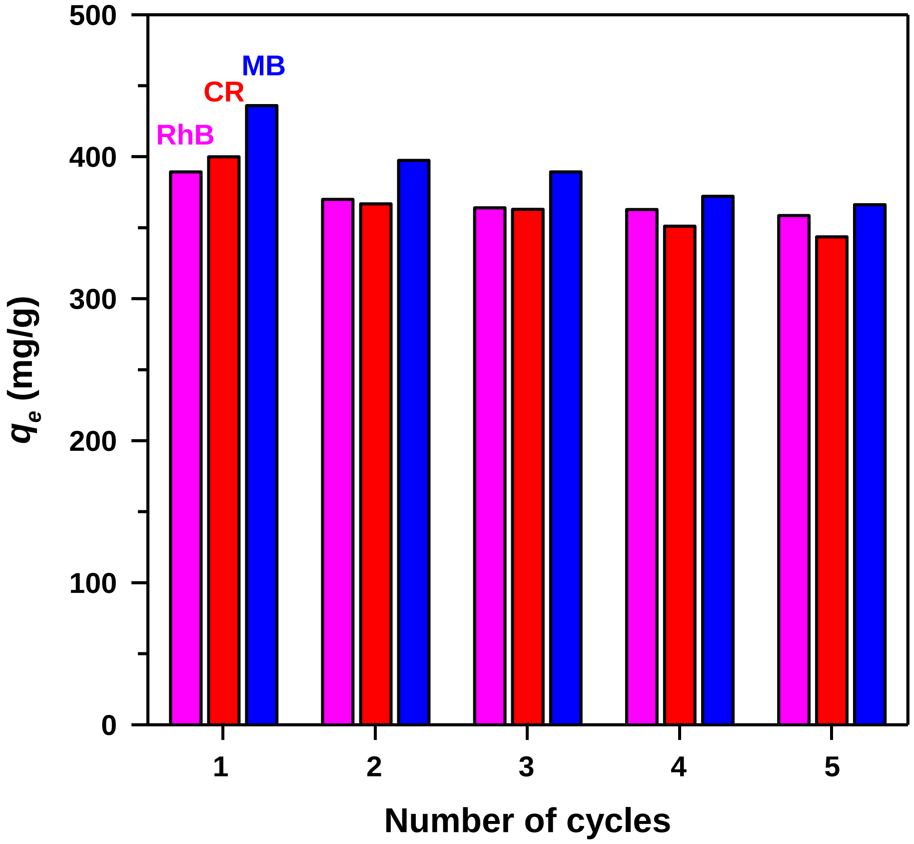

Figure S28. Reusability plot based on the changes in q_e values of *mM*-NC-200 for adsorption of large dye molecules.

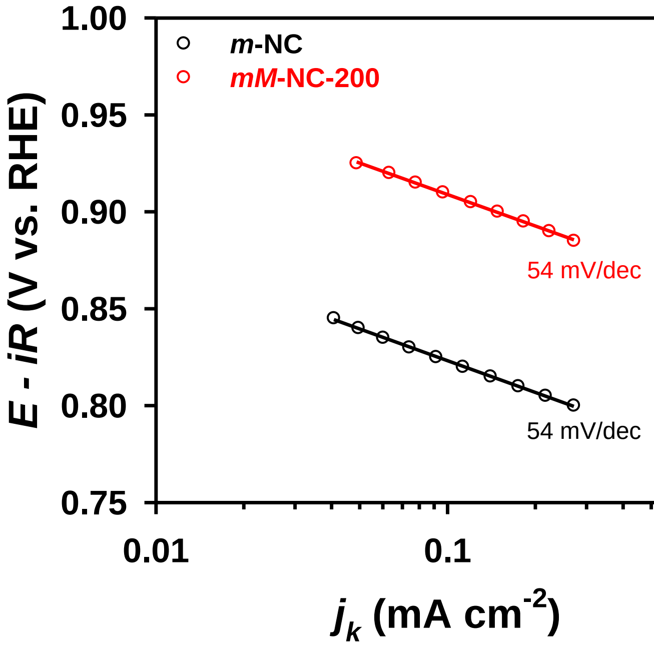

Figure S29. Tafel plots of *m*-NC and *mM*-NC-200 for the ORR.

References for ESI

1. F. Hayeeye, M. Sattar, W. Chinpa, O. Sirichote, *Colloids Surf. A: Physicochem. Eng. Aspects* **2017**, *513*, 259.
2. Y. Xie, W. Yang, M. Wang, X. Ge, *Chem. Eng. J.* **2017**, *323*, 224.
3. K. Liu, H. Li, Y. Wang, X. Gou, Y. Duan, *Colloids Surf. A: Physicochem. Eng. Aspects* **2015**, *477*, 35.
4. L. Chen, T. Ji, L. Brisbin, J. Zhu, *ACS Appl. Mater. Interfaces* **2015**, *7*, 12230.
5. B. H. Hammed, A. L. Ahmad, K. N. A. Latiff, *Dyes Pigments* **2007**, *75*, 143.
6. Y. Yao, F. Xu, M. Chen, Z. Xu, Z. Zhu, *Bioresource Technol.* **2010**, *101*, 3040.
7. A. L. Ahmad, M. M. Loh, J. A. Aziz, *Dyes Pigments* **2007**, *75*, 263.
8. A. Aijaz, N. Fujiwara, Q. Xu, *J. Am. Chem. Soc.*, **2014**, *136*, 6790.
9. L. Zhang, Z. Su, F. Jiang, L. Yang, J. Qian, Y. Zhou, W. Li, M. Hong, *Nanoscale*, **2014**, *6*, 6590.
10. H. Zhang, J. Wang, Y. Zhang, W. Xu, W. Xing, Y. Zhang, X. Zhang, *Angew. Chem. Int. Ed.*, **2014**, *53*, 14235.
11. P. Zhang, F. Sun, Z. Xiang, Z. Shen, J. Yun, D. Cao, *Energy Environ. Sci.*, **2014**, *7*, 442.
12. D. Zhao, J.-L. Shui, L. R. Grabstanowicz, C. Chen, S. M. Commet, T. Xu, J. Lu, D.-J. Liu, *Adv. Mater.*, **2014**, *26*, 1093.
13. S. Pandiaraj, H. B. Aiyappa, R. Banerjee, S. Kurungot, *Chem. Commun.*, **2014**, *50*, 3363.
14. Q. Lai, Y. Zhao, Y. Liang, J. He, J. Chen, *Adv. Mater.*, **2016**, *26*, 8334.
15. B. Y. Xia, Y. Yan, N. Li, H. B. Wu, X. W. Lou, X. Wang, *Nat. Energy*, **2016**, *1*, 15006.
16. L. Li, P. Dai, X. Gu, Y. Wang, L. Yan, X. Zhao, *J. Mater. Chem. A*, **2017**, *5*, 789.
17. R. Zhao, W. Xia, C. Lin, J. Sun, A. Mahmood, Q. Wang, B. Qiu, H. Tabassum, R. Zou, *Carbon*, **2017**, *114*, 284.